Research article **Open Access**

Zhen Chai, Xiaoyong Hu*, Hong Yang and Qihuang Gong*

Chip-integrated all-optical diode based on nonlinear plasmonic nanocavities covered with multicomponent nanocomposite

DOI 10.1515/nanoph-2016-0127
Received July 24, 2016; revised August 28, 2016; accepted September 1, 2016

Abstract: Ultracompact chip-integrated all-optical diode is realized experimentally in a plasmonic microstructure, consisting of a plasmonic waveguide side-coupled two asymmetric plasmonic composite nanocavities covered with a multicomponent nanocomposite layer, formed directly in a plasmonic circuit. Extremely large optical nonlinearity enhancement is obtained for the multicomponent nanocomposite cover layer, originating from resonant excitation, slow-light effect, and field enhancement effect. Nonreciprocal transmission was achieved based on the difference in the shift magnitude of the transparency window centers of two asymmetric plasmonic nanocavities induced by the signal light, itself, for the forward and backward propagation cases. An ultralow threshold incident light power of 145 μW (corresponding to a threshold intensity of 570 kW/cm^2) is realized, which is reduced by seven orders of magnitude compared with previous reports. An ultrasmall feature size of 2 μm and a transmission contrast ratio of 15 dB are obtained simultaneously.

Keywords: plasmonic nanocavity; all-optical diode; plasmon-induced transparency; third-order optical nonlinearity; multicomponent nanocomposite.

***Corresponding authors: Xiaoyong Hu and Qihuang Gong,** State Key Laboratory for Mesoscopic Physics and Department of Physics, Collaborative Innovation Center of Quantum Matter, Peking University, Beijing 100871, China; and Collaborative Innovation Center of Extreme Optics, Shanxi University, Taiyuan 030006, China, e-mail: xiaoyonghu@pku.edu.cn (X. Hu), qhgong@pku.edu.cn (Q. Gong)
Zhen Chai: State Key Laboratory for Mesoscopic Physics and Department of Physics, Collaborative Innovation Center of Quantum Matter, Peking University, Beijing 100871, China
Hong Yang: State Key Laboratory for Mesoscopic Physics and Department of Physics, Collaborative Innovation Center of Quantum Matter, Peking University, Beijing 100871, China; and Collaborative Innovation Center of Extreme Optics, Shanxi University, Taiyuan 030006, China

Ultracompact chip-integrated all-optical diode, possessing unique nonreciprocal transmission properties, is an essential and core component of optical computing system, ultrahigh-speed information processing chips, and optical communication networks [1]. For the practical on-chip integration applications, the all-optical diode should possess the following key characteristics: ultrasmall feature size, ultralow threshold power, high isolation ratio, and on-chip trigger [2, 3]. The basic idea of realizing chip-integrated all-optical diode is to break the time-reversal symmetry by using indirect interband photonic transition [4–7], angular-momentum biasing [8], magneto-optic effect [9–14], third-order optical nonlinearity [15–18], in dielectric photonic microstructures with broken spatial-reversal symmetry, including asymmetric photonic crystal heterostructures and asymmetric silicon ring resonators [19, 20]. The large size of dielectric photonic microstructures limits the practical on-chip integration applications of an all-optical diode [21]. Moreover, owing to the relatively small third-order nonlinear optical susceptibility of conventional organic and semiconductor materials, the threshold operation intensity is as high as GW/cm^2 order for the all-optical dielectric diode realized based on third-order optical nonlinearity [15–20]. Plasmonic microstructures possess the unique ability of confining light into deep-subwavelength scale and strong field reinforcement effect, which provides an excellent platform for the realization of nanoscale chip-integrated photonic devices [22]. Various schemes have been proposed to demonstrate chip-integrated all-optical diode in plasmonic microstructures, such as using graded plasmonic chains based on full retardation effect [23, 24], magnetized spiral chains of plasmonic ellipsoids based on interplay between the Faraday rotation and the geometrical spiral rotation under excitation of a longitudinal magnetic field [25], one-way electromagnetic modes at the interface between two dissimilar plasmonic metals (or a dielectric photonic crystal and a plasmonic metal) under excitation of a static magnetic field [26, 27], or nonlinear plasmonic crystals [28], In 2011, Fan et al. reported

an electromagnetic diode with a transmission contrast of 14.7 dB in a microwave transmission line consisting of three metallic ring resonators and a varactor [29]. In 2013, Sun et al. achieved an electromagnetic diode with a transmission contrast of 17.36 dB in a microwave waveguide system with asymmetric absorption and a varactor as a nonlinear medium [16]. However, up to now, little attention has been paid to the chip-integrated all-optical diodes based on plasmonic microstructures in the near-infrared and optical communication ranges.

Here, we report the realization of a nanoscale chip-integrated all-optical diode with an ultralow threshold power and ultrasmall feature size in a plasmonic microstructure etched directly in a plasmonic circuit operating in the near-infrared range. The plasmonic microstructure consisted of a plasmonic waveguide side-coupled two asymmetric plasmonic composite nanocavities covered with a 150-nm-thick multicomponent nanocomposite layer made of poly[2-methoxy-5-(2-ethylhexyloxy)-1,4-phenylenevinylene] (MEH-PPV) doped with organic chromophore IR140 and gold nanoparticles (nano-Au:(IR140:MEH-PPV)). Wang et al. and Lu et al. have pointed that a composite plasmonic microcavity could provide multiple microcavity resonance modes [30, 31]. Piao et al. also noted that a microcavity mode strongly coupled to the bus waveguide forms a superradiant mode, while a microcavity mode weakly coupled to the bus waveguide forms a subradiant mode [32]. The destructive interference coupling between the two excitation pathways (direct excitation of the superradiant microcavity mode, and then excitation of the subradiant microcavity mode through the superradiant microcavity mode) could produce on-chip plasmon-induced transparency in plasmonic circuits [33]. The multicomponent nanocomposite nano-Au:(IR140:MEH-PPV) provided a large third-order optical nonlinearity due to enormously strong nonlinearity enhancement associated with resonant excitation, slow-light effect, and field enhancement effect provided by plasmonic microcavity modes. Nonreciprocal transmission was achieved based on the difference in the shift magnitude of the transparency window centers of two asymmetric plasmonic nanocavities induced by the signal light, itself, for the forward and backward propagation cases. An ultralow threshold incident light power of 145 μW (corresponding to a threshold intensity of 570 kW/cm^2) is realized, which is reduced by seven orders of magnitude compared with previous reports [15–20]. An ultrasmall feature size of 2 μm and an isolation ratio of 15 dB are obtained simultaneously. This work not only provides an on-chip platform for the foundational study of nonlinear optics and quantum optics but also paves the way for the realization of ultrahigh-speed information processing chips based on plasmonic circuits.

The plasmonic microstructure, consisting of two nanocavities with a depth of 150 nm, was side-coupled to a bus plasmonic waveguide etched in a 300-nm-thick gold film deposited on a SiO_2 substrate, as shown in Figure 1A. Both the width and depth of the plasmonic waveguide were 150 nm. The nanocavity C1 was formed by two asymmetrically crossed nanogrooves. The length and width were 330 and 150 nm for the horizontal nanogroove in the Y and X direction, and 320 and 150 nm for the vertical nanogroove in the X and Y direction. The distance between the centers of the horizontal and vertical nanogrooves was 35 nm in the vertical direction and 40 nm in the horizontal direction. The nanocavity C2 was also formed by two asymmetrically crossed nanogrooves. The difference between the horizontal nanogrooves in the nanocavity C1 and C2 was the length of the horizontal nanogroove in C1, which is 50 nm less than that of C2. The size of the vertical nanogroove in the nanocavity C2 is the same as the one in C1. The distance between the centers of the horizontal and vertical nanogrooves was 35 nm in the vertical direction and 70 nm in the horizontal direction. The distance between nanocavities C1 and C2 was 2 μm. The 300-nm-thick gold film was fabricated by using a laser molecular beam epitaxy growth system (Model LMBE 450, SKY Company, China). The beam (with a wavelength of 248 nm and a pulse width of 25 ns) output from an excimer laser system (Model COMPexPro 205, Coherent Company, USA) was used as the light source. A focused ion beam etching system (Model Helios NanoLab 600, FEI Company, USA) was used to prepare the plasmonic microstructure. The scanning electron microscopy (SEM) image of the plasmonic microstructure sample without the multicomponent nanocomposite cover layer is shown in Figure 1B. To effectively excite and collect the required surface plasmon polaritons (SPPs), we fabricated a coupling grating etched through the gold film, connected to a 150-nm-deep triangular air groove in the input port of the plasmonic waveguide. The photon-to-SPP coupling efficiency of the input-coupling grating was more than 7% in a wideband wavelength range from 740 to 860 nm. A decoupling grating with a depth of 150 nm was also etched in the output port of the plasmonic waveguide to help couple the SPP mode into free space for the purpose of measurement. We also calculated the power density profile of the SPP mode in the plasmonic composite nanocavity C1 having the multicomponent nanocomposite cover layer excited by an 800-nm continuous-wave (CW) incident light using the finite element method (adopting a commercial software COMSOL Multiphysics) [33], and the

calculated results are shown in Figure 1C. The guided SPP mode was mainly confined in the nanogroove region and extended into the upper multicomponent nanocomposite cover layer, which indicates that the plasmonic nanocavity resonance modes are very sensitive to the refractive index change of the multicomponent nanocomposite cover layer. The doping concentration was 15% for IR140 and 20% for gold nanoparticles in the multicomponent nanocomposite nano-Au:(IR140:MEH-PPV). The gold nanoparticles have a configuration of nanoflowers, having a solid core connected with abundant spike-shaped tips with a length ranging from 10 to 20 nm, as shown in Figure 1D. The measured linear absorption spectrum of the gold nanoparticle colloid is shown in Figure 1E. There is a broad linear absorption band ranging from 500 to 900 nm, centered at 750 nm, which corresponds to the surface plasmon resonance (SPR) wavelength of gold nanoparticles [34]. The measured linear absorption spectrum of a 150-nm-thick organic IR140:MEH-PPV film is shown in Figure 1F. Two linear absorption bands, one ranging from 200 to 580 nm (originating from the linear absorption of MEH-PPV) [35], while another ranging from 650 to 880 nm (originating from the linear absorption of IR140) [36], were obtained. The SPR peak of gold nanoparticles drops in the linear absorption band of IR140. Measured closed-aperture Z-scan curves of a 150-nm-thick nano-Au:(IR140:MEH-PPV) multicomponent nanocomposite layer by using a 120-fs, 800-nm laser beam. The value of the nonlinear refractive index was measured to be -1.3×10^{-4} cm^2/kW, which is eight orders of magnitude larger than that of SiO_2, 1×10^{-12} cm^2/kW [37]. This means that the multicomponent nanocomposite nano-Au:(IR140:MEH-PPV) has excellent third-order optical nonlinearity. We also measured the closed aperture Z-scan data measured at different incident

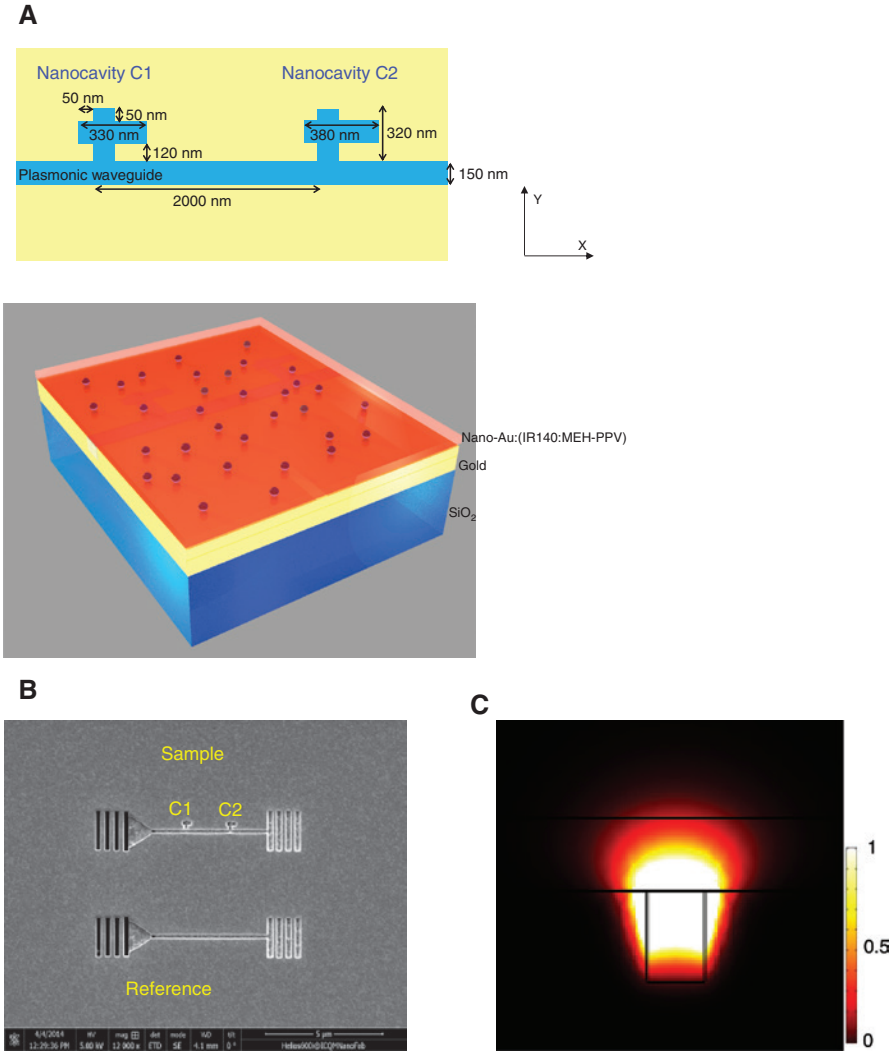

Figure 1 (continued)

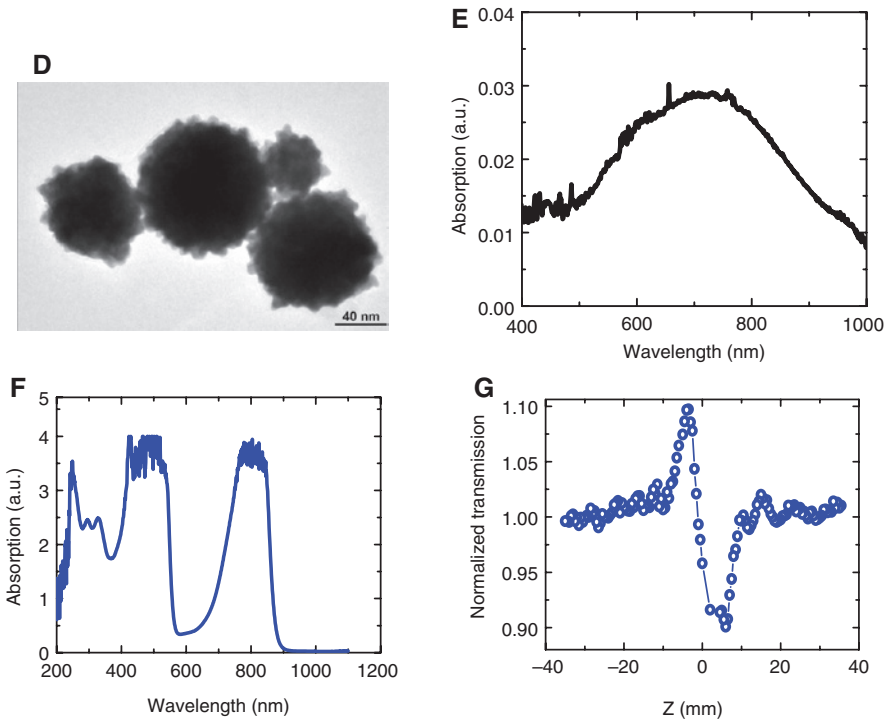

Figure 1: (A) Top view schematic diagram (upper) of the plasmonic microstructure without the nano-Au:(IR140:MEH-PPV) cover layer and three-dimensional schematic structure (lower) of the plasmonic microstructure having the nano-Au:(IR140:MEH-PPV) cover layer. (B) SEM image of the plasmonic microstructure sample and the reference waveguide, without the nano-Au:(IR140:MEH-PPV) cover layer. (C) Calculated power density profile of the SPP mode in the plasmonic composite nanocavity C1 with the nano-Au:(IR140:MEH-PPV) cover layer excited by 800 nm CW incident light. (D) TEM image of gold nanoparticles in the IR140:MEH-PPV composite polymer matrix. Measured linear absorption spectrum of gold nanoparticle colloid (E) and a 150-nm-thick organic IR140:MEH-PPV film (F). (G) Measured closed-aperture Z-scan curves of a 150-nm-thick nano-Au:(IR140:MEH-PPV) cover layer by using a 120-fs, 800-nm laser.

powers, and the same value of the nonlinear refractive index was obtained. Quarterman et al. have pointed out that as an intrinsic material parameter, the value of the nonlinear refractive index was independent of the incident light power [38].

To study the on-chip plasmon-induced transparency provided by the plasmonic composite nanocavity C1, we measured the linear transmission spectra of the plasmonic waveguide side-coupled plasmonic composite nanocavity C1 having the multicomponent nanocomposite nano-Au:(IR140:MEH-PPV) cover layer by using a microspectroscopy measurement system [33]. A p-polarized CW Ti:sapphire laser system (Model Mira 900F, Coherent Company, USA) was used as the light source. The line width of the laser spectrum curve was only 1.7 nm, which ensures that only the required quasi-monochromatic SPP mode can be excited in the plasmonic waveguide. The coupling grating was normally illuminated from the back side. The optically thick gold film can prohibit direct transmission of the incident laser beam. The SPP mode that propagated through the plasmonic waveguide was scattered using the decoupling grating in the output port. The scattered light was collected using a long working distance objective (Mitutoyo 20, NA = 0.58) and then imaged using a charge-coupled device (CCD). The linear transmission was normalized with respect to a reference straight plasmonic waveguide, as shown in Figure 2A, which is the standard method used to study the linear transmission properties of plasmonic microcavities [39]. The spot size of the incident laser beam was 9 μm, which ensures nearly equal average excitation intensities for the coupling gratings of both the composite nanocavity sample and the reference waveguide. Limited by the tunable wavelength range of the Ti:sapphire laser system, we only measured the linear transmission spectrum in the wavelength range changing from 700 to 900 nm. A sharp and high transmission peak appeared in the transmission forbidden band, which implies the formation of plasmon-induced transparency, as shown in Figure 2B. Wang et al. and Lu et al. have pointed that a composite plasmonic microcavity could provide multiple microcavity resonance modes [30, 31]. Piao et al. also noted that a microcavity mode strongly coupled to the bus waveguide forms a superradiant mode, while a microcavity mode weakly coupled to the bus

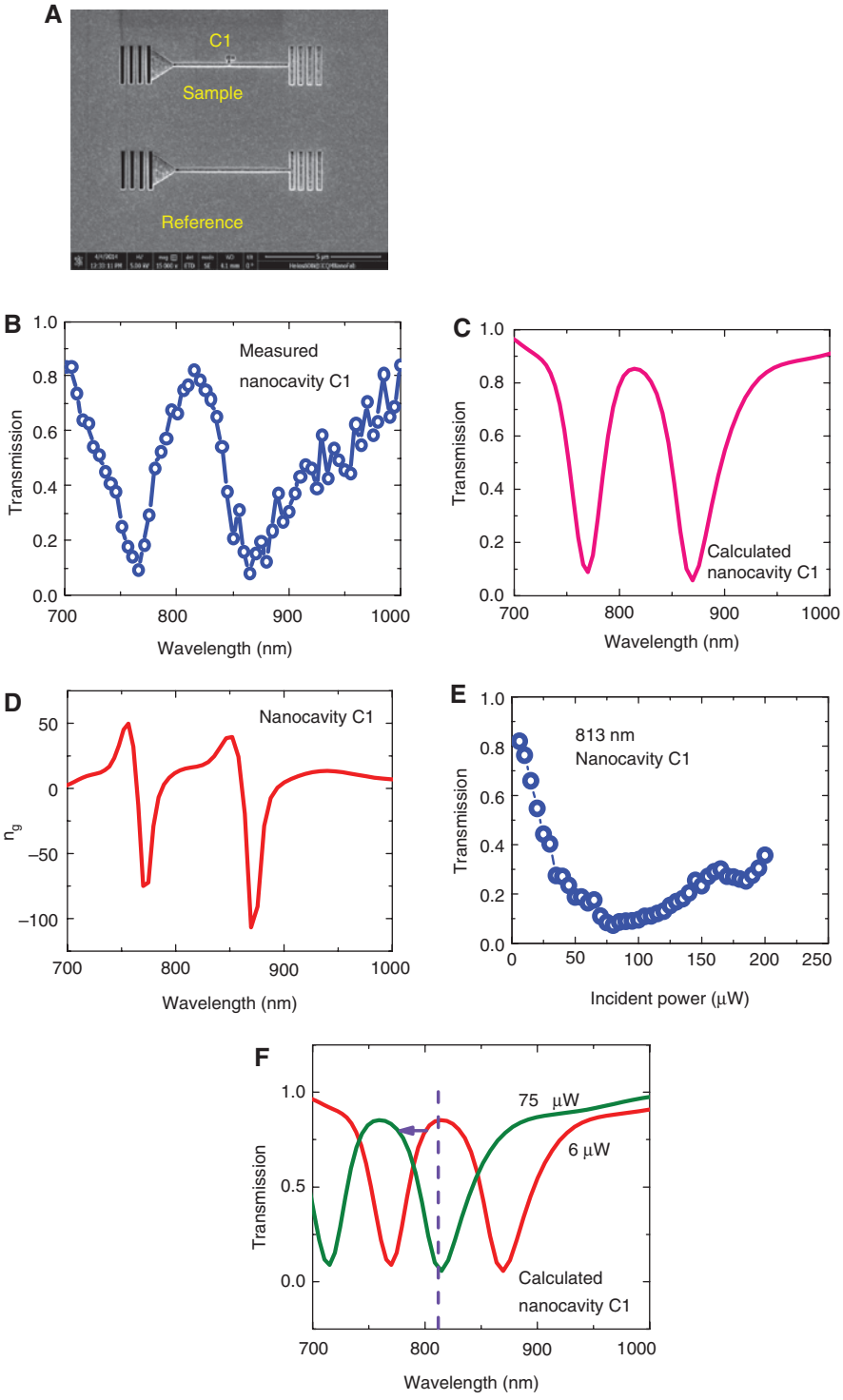

Figure 2: (A) SEM image of the plasmonic composite nanocavity C1 and the Reference waveguide, without the nano-Au:(IR140:MEH-PPV) cover layer. Measured (B) and calculated (C) linear transmission spectra of the plasmonic waveguide side coupled the plasmonic composite nanocavity C1 having the nano-Au:(IR140:MEH-PPV) cover layer. (D) Calculated group refractive index as a function of incident light wavelength for the plasmonic waveguide side coupled plasmonic composite nanocavity C1 having the nano-Au:(IR140:MEH-PPV) cover layer. (E) Measured transmission changes of the 813-nm incident light as a function of incident power in the plasmonic waveguide side coupled plasmonic composite nanocavity C1 having the nano-Au:(IR140:MEH-PPV) cover layer. (F) Calculated linear transmission spectra of the plasmonic waveguide side coupled the plasmonic composite nanocavity C1 having the nano-Au:(IR140:MEH-PPV) cover layer for a different incident power.

waveguide forms a subradiant mode [32]. The destructive interference coupling between the two excitation pathways (direct excitation of the superradiant microcavity mode, and then excitation of the subradiant microcavity mode through the superradiant microcavity mode) could produce on-chip plasmon-induced transparency in plasmonic circuits [33]. The central wavelength and the peak transmission of the transparency window were 813 nm and 82%, respectively, which are in good agreement with the values calculated using the finite element method, as shown in Figure 2C. To confirm the slow light effect around the transparency window, we calculated the group refractive index as a function of incident light wavelength for the plasmonic waveguide side-coupled plasmonic composite nanocavity C1 having the nano-Au:(IR140:MEH-PPV) cover layer, and the calculated results are shown in Figure 2D. It is very clear that excellent slow-light effect could be achieved around the transparency window. To study the all-optical tunability of the plasmon-induced transparency, we measured transmission changes of the 813-nm, 120-fs incident light (with a pulse repetition rate of 76 MHz) as a function of incident power in the plasmonic waveguide side-coupled plasmonic composite nanocavity C1 having the nano-Au:(IR140:MEH-PPV) cover layer, and the measured results are shown in Figure 2E. When the incident power increased from 6 to 75 μW, the transmission of the incident light decreased from 82% to 10%. The wavelength of 813 nm was located in the center of the transparency window. According to the third-order nonlinear optical Kerr effect, the effective refractive index n of nano-Au:(IR140:MEH-PPV) can be calculated by [40]

$$n = n_0 + n_2 I = n_0 + \frac{3\mathrm{Re}\,\chi^{(3)}}{4\varepsilon_0 c n_0^2} I \tag{1}$$

where n_0, n_2, and $\mathrm{Re}\chi^{(3)}$ are linear and nonlinear refractive indices, and real part of the third-order nonlinear susceptibility of the nanocomposite material, respectively. ε_0 is the permittivity of a vacuum, c is the light velocity in a vacuum, I is the pump intensity. Owing to the negative value of the multicomponent nanocomposite nano-Au:(IR140:MEH-PPV), the refractive index of nano-Au:(IR140:MEH-PPV) decreased with the increase in the incident light power, which makes the resonance modes provided by the plasmonic nanocavity C1 shifts in the short wavelength. As a result, the transparency window center shifts in the short wavelength direction, and subsequently, the incident light transmission decreases. When the incident power was 75 μW, the transmission minimum in the long-wavelength direction shifted to the position of 813 nm, as shown in Figure 2F. When the incident power was larger than 75 μW, the transmission of 813-nm incident light increased. The wavelength of 813 nm situated in the linear absorption band of the organic chromophore and around the surface plasmon resonance (SPR) peak of gold nanoparticles, as shown in Figure 1E and F. Therefore, the resonant excitation contributes to the nonlinearity enhancement of nano-Au:(IR140:MEH-PPV) cover layer. The excellent slow light effect (shown in Figure 2D) around the transparency window also dedicates to the nonlinearity enhancement of nano-Au:(IR140:MEH-PPV) cover layer. Moreover, the strong field reinforcement of the nanocavity mode (shown in Figure 1C) also contributes to the nonlinearity enhancement of nano-Au:(IR140:MEH-PPV) cover layer. This results in an extremely large nonlinear refractive index of nano-Au:(IR140:MEH-PPV), which is confirmed by our closed-aperture Z-scan measurement (shown in Figure 1G).

To study the on-chip plasmon-induced transparency provided by the plasmonic composite nanocavity C2, we measured the linear transmission spectra of the plasmonic waveguide side-coupled plasmonic composite nanocavity C2 having the nano-Au:(IR140:MEH-PPV) cover layer by using the microspectroscopy measurement system [33]. The basic linear properties and physical mechanism are almost identical with that of C1. The measured linear transmission in Figure 3A implies the formation of plasmon-induced transparency, as shown in Figure 3B. The central wavelength and the peak transmission of the transparency window were 825 nm and 78%, respectively, matching the values calculated using the finite element method (Figure 3C). Similar with the nonlinear measurement methods of the plasmonic composite nanocavity C1, we also measured transmission changes with incident power of the whole nanocavity C1 structure at the wavelength of the 790 nm, located in the transmission minimum in the short wavelength, to study the all-optical tunability of the plasmon-induced transparency, and the measured results are shown in Figure 3D. The transmission of the incident light increased from 10% to 78%, while the incident power increased from 6 to 120 μW. The nanocomposite nano-Au:(IR140:MEH-PPV) has a negative value of nonlinear refractive index in the near-infrared range. Therefore, the refractive index n of the nanocomposite decreases with the increase in the photon energy, which lead to the blue shift in the nanocavity resonance frequency to the reduction in the refractive index of nano-Au:(IR140:MEH-PPV) with increasing signal power. As a result, the transparency window center shifts in the short wavelength direction, and subsequently, the incident light transmission decreases. When the incident power was 120 μW, the transparency window center shifted to

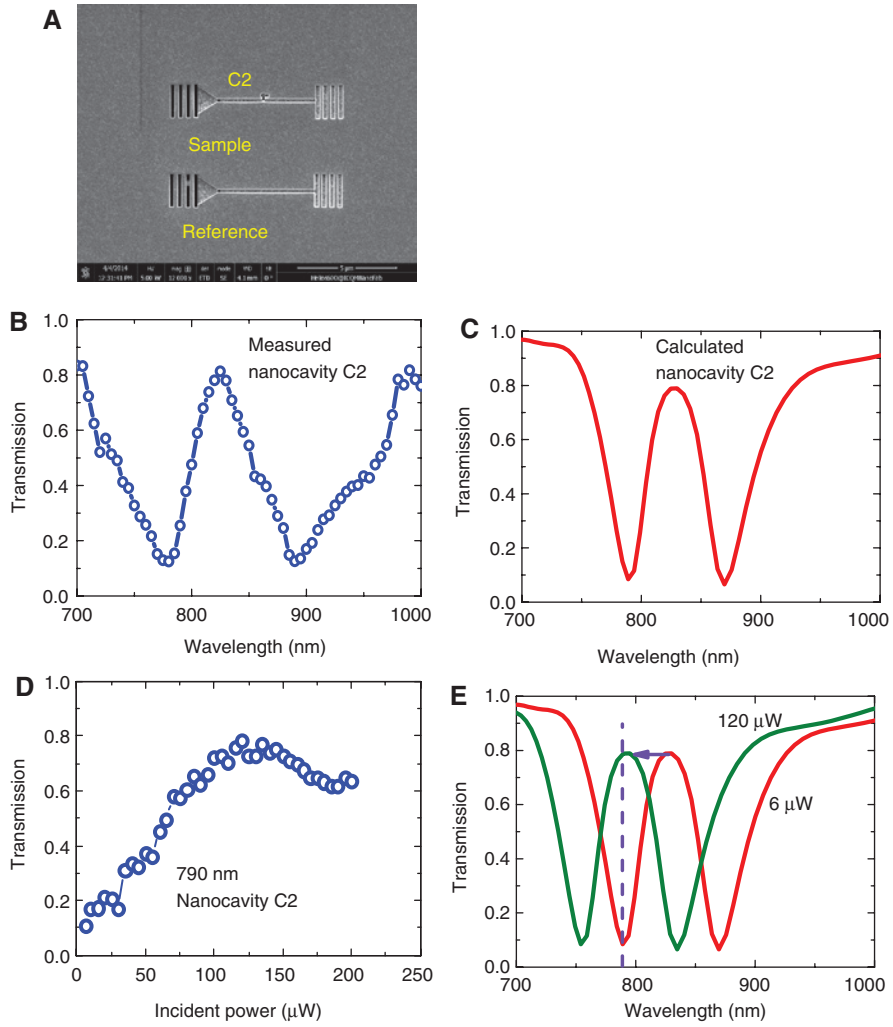

Figure 3: (A) SEM image of the plasmonic composite nanocavity C2 and the reference waveguide, without the nano-Au:(IR140:MEH-PPV) cover layer. Measured (B) and calculated (C) linear transmission spectra of the plasmonic waveguide side coupled the plasmonic composite nanocavity C2 having the nano-Au:(IR140:MEH-PPV) cover layer. (D) Measured transmission changes of the 790-nm incident light as a function of incident power in the plasmonic waveguide side coupled the plasmonic composite nanocavity C2 having the nano-Au:(IR140:MEH-PPV) cover layer. (E) Calculated linear transmission spectra of the plasmonic waveguide side coupled the plasmonic composite nanocavity C2 having the nano-Au:(IR140:MEH-PPV) cover layer for a different incident power.

the position of 790 nm, as shown in Figure 3E. When the incident power was larger than 120 μW, the transmission of an 813-nm incident light decreased. These indicate that the plasmon-induced transparency possesses excellent all-optical tunability under excitation of the signal light, itself.

To study the all-optical diode function, we measured transmission changes of the 795-nm incident light as a function of incident power in the plasmonic waveguide side-coupled plasmonic composite nanocavities C1 and C2 having the nano-Au:(IR140:MEH-PPV) cover layer for the C1–C2 propagation case, i.e. the signal light first propagating through the plasmonic composite nanocavity C1, and subsequently the plasmonic composite nanocavity C2, and the measured results are shown in Figure 4A. The transmission of the 795-nm signal light was less than 30% when the incident power increased from 6 to 200 μW. The wavelength of 795 nm situated near the transparency window center of the plasmonic nanocavity C1, and around the transmission minimum of the plasmonic nanocavity C2, as shown in Figures 2 and 3. For the C1–C2 propagation case, the signal light first reaches the position of the plasmonic composite nanocavity C1, which results in a remarkable blue shift in the center wavelength of the transparency window of the plasmonic composite nanocavity C1 with an increase in the incident power of the signal light. The length of the plasmonic waveguide between the nanocavities C1

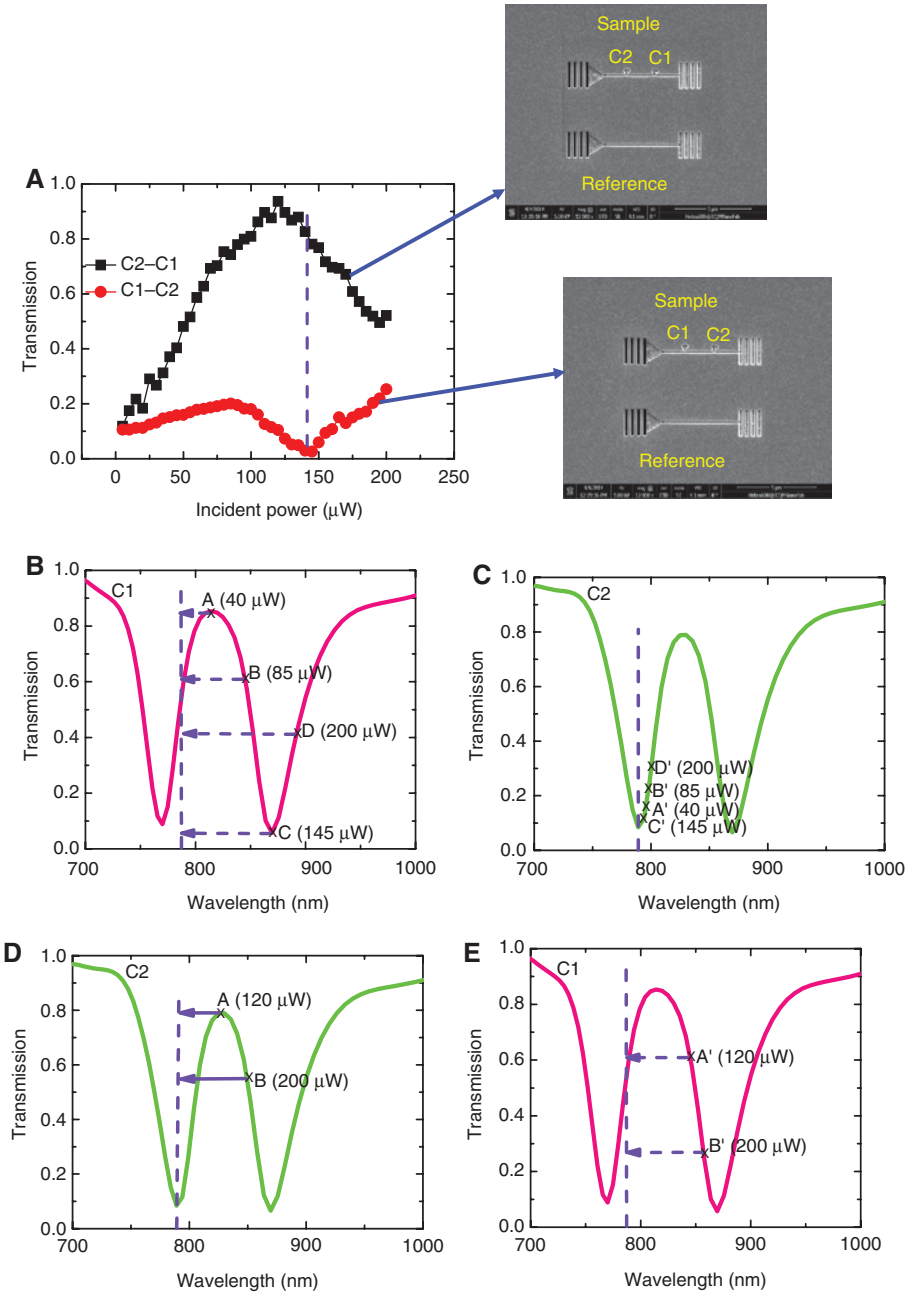

Figure 4: (A) Measured all-optical diode performance for a 795-nm incident light. The plasmonic microstructure samples used for the different propagation cases are shown on the right side. (B) Calculated linear transmission spectrum of a plasmonic waveguide side coupled plasmonic composite nanocavity C1 with the nano-Au:(IR140:MEH-PPV) cover layer for the C1–C2 propagation case. Arrows and crosses indicate which points shift to the position of 795 nm. (C) Calculated linear transmission spectrum of a plasmonic waveguide side coupled plasmonic composite nanocavity C2 with the nano-Au:(IR140:MEH-PPV) cover layer for the C1–C2 propagation case. Crosses indicate which points shift to the position of 795 nm. (D) Calculated linear transmission spectrum of a plasmonic waveguide side coupled plasmonic composite nanocavity C2 with the nano-Au:(IR140:MEH-PPV) cover layer for the C2–C1 propagation case. Arrows and crosses indicate which points shift to the position of 795 nm. (E) Calculated linear transmission spectrum of a plasmonic waveguide side coupled plasmonic composite nanocavity C1 with the nano-Au:(IR140:MEH-PPV) cover layer for the C2–C1 propagation case. Crosses indicate which points shift to the position of 795 nm.

and C2 was 2 μm, as shown in Figure 1A. According to our calculation, by using the finite element method, owing to the intrinsic propagation losses of the plasmonic waveguide, the signal light power P2 reaching the position of nanocavity C2 was 0.7P1, where P1 is the signal power just passing the position of the nanocavity C1.

As a result, limited by both the transmission properties of the nanocavity C1 and the propagation losses of the plasmonic waveguide, the signal light power reaching the position of the nanocavity C2 was reduced greatly. This results in a much smaller blue shift in the center wavelength of the transparency window of the plasmonic composite nanocavity C2 compared with that of the nanocavity C1, under excitation of an incident signal light. When the incident power increased from 6 to 85 μW for the C1–C2 propagation case, the transmission of the signal light increased from 10% to 20%, as shown in Figure 4A. When the incident power increased from 6 to 85 μW, the center region of the transparency window shifted to the position of 795 nm in the transmission spectrum of the plasmonic waveguide side coupled the nanocvity C1, as shown in Figure 4B. This results in that the signal power reaching the position of the nanocavity C2 increases with the increment of the incident power. When the incident power was 85 μW, the point B′ shifted to the position of 795 nm in the transmission spectrum of the plasmonic waveguide side-coupled the nanocvity C2, as shown in Figure 4C. This leads to a total transmission of 20% for the signal light propagating through the plasmonic microstructure. When the incident power increased from 85 to 145 μW for the C1–C2 propagation case, the transmission of the signal light decreased from 20% to 2.6%, as shown in Figure 4A. When the incident power increased from 85 to 145 μW, the position of 795 nm gradually reached the edge of the transparency window, which makes the signal power reaching the position of the nanocavity C2 smaller and smaller. When the incident power was 145 μW, the point C′ shifted to the position of 795 nm in the transmission spectrum of the plasmonic waveguide side coupled the nanocvity C2, as shown in Figure 4C, which leads to a very small total transmission for the signal light propagating through the plasmonic microstructure. When the incident power increased from 145 to 200 μW for the C1–C2 propagation case, the transmission of the signal light increased from 2.6% to 25%, as shown in Figure 4A. When the incident power increased from 145 to 200 μW, the wavelength of 795 nm reached the pass band of the nanocavity C2, which makes the signal power reaching the position of the nanocavity C2 increase with the increment of the incident power. When the incident power was 200 μW, the point D′, shifted to the position of 795 nm in the transmission spectrum of the plasmonic waveguide, side coupled the nanocvity C2, as shown in Figure 4C, which leads to a relatively large total transmission of the signal light propagating through the plasmonic microstructure.

We also measured that transmission changes of the 795-nm incident light as a function of incident power in the plasmonic waveguide side coupled the plasmonic composite nanocavities C2 and C1 having the nano-Au:(IR140:MEH-PPV) cover layer for the C2–C1 propagation case, i.e. the signal light first propagating through the plasmonic composite nanocavity C2 and, subsequently, the plasmonic composite nanocavity C1, and the measured results are shown in Figure 4A. When the incident power increased from 6 to 120 μW for the C2–C1 propagation case, the transmission of the signal light increased from 10% to 90%. For the C2–C1 propagation case, the signal light first reaches the position of the plasmonic composite nanocavity C2, which results in a remarkable blue shift in the center wavelength of the transparency window of the plasmonic composite nanocavity C2 with an increase in the incident power of the signal light. With the increase in the incident power, the transparency window center provided by the nanocvity C2 shifted toward the position of 795 nm, as shown in Figure 4D, which makes the signal light power reaching the position of nanocavity C1 increase with the increment of the incident power. When the incident power increased from 6 to 120 μW, even though the transparency window provided by the nanocavity C1 shifted in the short-wavelength direction, the wavelength of 795 nm still situated with the region near the transparency window center, as shown in Figure 4E. Therefore, the final transmission of the signal light propagating through the plasmonic microstructure increased with the increment of the incident power. When the incident power increased from 120 to 200 μW for the C2–C1 propagation case, the transmission of the signal light decreased from 90% to 40%. When the incident power increased from 120 to 200 μW, the transparency window center provided by the nanocvity C2 shifted away from the position of 795 nm, as shown in Figure 4D, which makes the signal light power reaching the position of nanocavity C1 decrease with the increment of the incident power. Moreover, when the incident power increased from 120 to 200 μW, the transparency window center provided by the nanocvity C1 also shifted away from the position of 795 nm, as shown in Figure 4E. This makes the transmission of the signal light propagating through the plasmonic microstructure decrease with the increment of the incident power. Therefore, for a 145-μW, 795-nm incident light, the transmission was 82% for the C2–C1 propagation case and 2.6% for the C1–C2 propagation case, which ensures that a transmission contrast ratio of 15 dB was obtained. An ultralow threshold incident light power of 145 μW (corresponding to a threshold intensity of 570 kW/cm^2) was realized, which is reduced by seven orders of magnitude compared with previous

reports [15–20]. An ultrasmall feature size of 2 μm was obtained simultaneously.

The operating wavelength of the diode action, i.e. 795 nm, dropped in the linear absorption band of IR140, was far away from the linear absorption band of MEH-PPV and was close to the SPR resonance wavelength of the gold nanoparticles, as shown in Figure 1F. Liebig et al. have pointed out that IR140 was an excellent saturable absorber under excitation of a femtosecond laser beam having a wavelength ranging from 650 to 900 nm, thus, widely used in passively mode locked Ti:sapphire laser systems [41]. Boni et al. also pointed out that MEH-PPV had a small value of two-photon absorption cross-section around 800 nm, about 4×10^{-47} cm^4 s/photon, while a maximum two-photon absorption cross-section located at 600 nm [42]. Grabar et al. also noted that the nonlinear absorption of gold nanoparticles could be neglected under SPR resonant excitation [34]. Moreover, the guided SPP mode was mainly confined in the nanogroove region and extended into the upper multicomponent nanocomposite nano-Au:(IR140:MEH-PPV) cover layer, as shown in Figure 1C. This means that only a small part of the incident light could reach the nano-Au:(IR140:MEH-PPV) cover layer. According to our measurement, the influences of the nonlinear absorption of IR140, MEH-PPV, and gold nanoparticles on the power reduction of the signal light propagating in the plasmonic circuits could be neglected [43]. Therefore, the nonlinear absorption of IR140, MEH-PPV, and gold nanoparticles can be ruled out at the operating wavelengths of the all-optical diode, and the diode action was very robust against the nonlinear effects like nonlinear absorption.

In conclusion, we have experimentally realized that an ultracompact chip-integrated all-optical diode is realized in a plasmonic microstructure etched in plasmonic circuits directly. An ultralow threshold incident light power of 145 μW is realized, which is reduced by seven orders of magnitude compared with previous reports. An ultrasmall feature size of 2 μm and a transmission contrast ratio of 15 dB are obtained simultaneously. This work not only provides an on-chip platform for the foundational study of nonlinear optics and quantum optics but also paves the way for the realization of ultrahigh-speed information processing chips based on plasmonic circuits.

Acknowledgments: This work was supported by the 973 Program of China under grant nos. 2013CB328704 and 2014CB921003, the National Natural Science Foundation of China under grant nos. 11225417, 61475003, 11134001, 11121091, and 90921008.

References

[1] Kang MS, Butsch A, Russell PSJ. Reconfigurable light-driven opto-acoustic isolators in photonic crystal fibre. Nat Photon 2011;5:549–53.
[2] Peng B, Ozdemir SK, Lei FC, et al. Parity–time-symmetric whispering-gallery microcavities. Nature Phys 2014;10:394–8.
[3] Chang L, Jiang XS, Hua SY, et al. Parity–time symmetry and variable optical isolation in active–passive-coupled microresonators. Nat Photon 2014:8:524–9.
[4] Yu ZF, Fan SH. Complete optical isolation created by indirect interband photonic transitions. Nat Photon 2009;3:91–4.
[5] Lira H, Yu ZF, Fan SH, Lipson M. Electrically driven nonreciprocity induced by interband photonic transition on a silicon chip. Phys Rev Lett 2012;109:033901.
[6] Feng L, Ayache M, Huang JQ, et al. Nonreciprocal light propagation in a silicon photonic circuit. Science 2011;333:729.
[7] Yu ZF, Fan SH. Optical isolation based on nonreciprocal phase shift induced by interband photonic transitions. Appl Phys Lett 2009;94:171116.
[8] Estep NA, Sounas DL, Soric J, Alu A. Magnetic-free non-reciprocity and isolation based on parametrically modulated coupled-resonator loops. Nat Phys 2014;10:923–7.
[9] Bi L, Hu JJ, Jiang P, et al. On-chip optical isolation in monolithically integrated non-reciprocal optical resonators. Nat Photon 2011;5:758–62.
[10] Tamagnone M, Fallahi A, Mosig JR, Perruisseau-Carrier J. Fundamental limits and near-optimal design of graphene modulators and non-reciprocal devices. Nat Photon 2014;8:556–63.
[11] Haldane FDM, Raghu S. Possible realization of directional optical waveguides in photonic crystals with broken time-reversal symmetry. Phys Rev Lett 2008;100:013904.
[12] Wang Z, Chong YD, Joannopoulos JD, Soljacic M. Reflection-free one-way edge modes in a gyromagnetic photonic crystal. Phys Rev Lett 2008;100:013905.
[13] Poo Y, Wu RX, Lin ZF, Yang Y, Chan CT. Experimental realization of self-guiding unidirectional electromagnetic edge states. Phys Rev Lett 2011;106:093903.
[14] Wang Z, Chong YD, Joannopoulos JD, Soljacic M. Observation of unidirectional backscattering-immune topological electromagnetic states. Nature 2009;461:772–5.
[15] Fan L, Wang J, Varghese LT, et al. An all-silicon passive optical diode. Science 2012;335:447–50.
[16] Sun Y, Tong YW, Xue CH, et al. Electromagnetic diode based on nonlinear electromagnetically induced transparency in metamaterials. Appl Phys Lett 2013;103:091904.
[17] Anand B, Podila R, Lingam K, et al. Optical diode action from axially asymmetric nonlinearity in an all-carbon solid-state device. Nano Lett 2013;13:5771–6.
[18] Shi Y, Yu ZF, Fan SH. Limitations of nonlinear optical isolators due to dynamic reciprocity. Nat Photon 2015;9:388–92.
[19] Jalas D, Petrov A, Eich M, et al. What is – and what is not – an optical isolator. Nat Photon 2013;7:579–82.
[20] Hu XY, Li ZQ, Zhang JX, Yang H, Gong QH, Zhang XP. Low-power and high-contrast nanoscale all-optical diodes via nanocomposite photonic crystal microcavities. Adv Funct Mater 2011;21:1803–9.

[21] Yin XB, Zhang X. Unidirectional light propagation at exceptional points. Nat Mater 2013;12:175–7.
[22] Schuller JA, Barnard ES, Cai WS, Jun YC, White JS, Brongersma ML. Plasmonics for extreme light concentration and manipulation. Nat Mater 2010;9:193–204.
[23] Zheng MJ, Lei DY, Yakubo K, Yu W. Asymmetric propagation of optical signals in graded plasmonic chains. Plasmonics 2011;6:19–27.
[24] Malyshev AV, Maalyshev VA, Knoester J. Frequency-controlled localization of optical signals in graded plasmonic chains. Nano Lett 2008;8:2369–72.
[25] Hadad Y, Steinberg BZ. Magnetized spiral chains of plasmonic ellipsoids for one-way optical waveguides. Phys Rev Lett 2010;105:233904.
[26] Dixit M, Stroud D. Realization of one-way electromagnetic modes at the interface between two dissimilar metals. Appl Phys Lett 2014;104:061604.
[27] Yu ZF, Veronis G, Wang Z, Fan SH. One-way electromagnetic waveguide formed at the interface between a plasmonic metal under a static magnetic field and a photonic crystal. Phys Rev Lett 2008;100:023902.
[28] Keshmarzi EK, Tait RN, Berini P. Spatially nonreciprocal Bragg gratings based on surface plasmons. Appl Phys Lett 2014;105:191110.
[29] Fan YC, Han J, Wei ZY, et al. Subwavelength electromagnetic diode: one-way response of cascading nonlinear meta-atoms. Appl Phys Lett 2011;98:151903.
[30] Wang TB, Wen XW, Yin CP, Wang HZ. The transmission characteristics of surface plasmon polaritons in ring resonator. Opt Express 2009;17:24096–101.
[31] Lu H, Liu XM, Mao D, Wang L, Gong YK. Tunable band-pass plasmonic waveguide filters with nanodisk resonators. Opt Express 2010;18:17922–7.
[32] Piao X, Yu S, Park N. Control of Fano asymmetry in plasmon induced transparency and its application to plasmonic waveguide modulator. Opt Express 2012;20:18994–9.
[33] Chai Z, Hu XY, Zhu Y, Sun SB, Yang H, Gong QH. Ultracompact chip-integrated electromagnetically induced transparency in a single plasmonic composite nanocavity. Adv Optical Mater 2014;2:320–5.
[34] Grabar KC, Freeman RG, Hommer MB, Natan MJ. Preparation and characterization of Au colloid monolayers. Anal Chem 1995;67:735–43.
[35] Oliveira SL, Correa DS, Boni LD, Misoguti L, Zilio SC, Mendonca CR. Two-photon absorption cross-section spectrum of a ππ-conjugated polymer obtained using the white-light continuum Z-scan technique. Appl Phys Lett 2006;88:021911.
[36] Decker CD. Excited state absorption and laser emission from infrared laser dyes optically pumped at 532 nm. Appl Phys Lett 1975;27:607.
[37] Miller A, Welford KR, Daino B. Nonlinear optical materials and devices for application in information technology, The Netherlands, Kluwer Academic, 1992.
[38] Quarterman AH, Tyrk MA, Wilcox KG. Z-scan measurements of the nolinear refractive index of a pumped semiconductor disk laser gain medium. Appl Phys Lett 2015;106:011105.
[39] Han ZH, Ortiz CEG, Radko IP, Bozhevolnyi SI. Detuned-resonator induced transparency in dielectric-loaded plasmonic waveguides. Opt Lett 2013;36:875–7.
[40] Boyd RW. Nonlinear optics, San Diego, USA, Academic Press Inc., 1992.
[41] Liebig CM, Dennis WM. Optical dephasing in saturable-absorbing organic dye IR140. Appl Opt 2006;45:2072–6.
[42] Boni LD, Andrade AA, Correa DS, et al. Nonlinear absorption spectrum in MEH-PPV/chloroform solution: a competition between two-photon and saturated absorption process. J Phys Chem B 2004;108:5221–4.
[43] Chai Z, Zhu Y, Hu XY, et al. On-chip optical switch based n plasmon-photon hybrid nanostructure-coated multicomponent nanocomposite. Adv Optical Mater 2016;4:1159–66.

Supplemental Material: The online version of this article (DOI: 10.1515/nanoph-2016-0127) offers supplementary material, available to authorized users.